Lin *et al. Soft Sci.* **2025**, *5*, 47
DOI: 10.20517/ss.2025.53

Soft Science

Research Article

Open Access

Check for updates

Island-bridge microstructured triboelectric pressure sensor for effective dynamic epidermal pulse monitoring

Zhiming Lin[1,2,*], Yiming Wang[1,2], Shijin Nie[1], Mingjun Zou[2], Fang Xu[2], Yulong Deng[2], Yanpeng Lu[2], Lincan Deng[3], Min Li[1], Guoxi Luo[1], Tao Dong[1], Libo Zhao[1], Hengyu Guo[4]

[1]School of Instrument Science and Technology, Xi'an Jiaotong University, Xi'an 710049, Shaanxi, China.
[2]Yibin Academy of Southwest University, Yibin 644000, Sichuan, China.
[3]International Engineering Company, CNPC Chuanqing Drilling Engineering Company Limited, Chengdu 610056, Sichuan, China.
[4]School of Physics, Chongqing University, Chongqing 400044, China.

[*]**Correspondence to:** Prof. Zhiming Lin, School of Instrument Science and Technology, Xi'an Jiaotong University, Xi'an 710049, Shaanxi, China. E-mail: zhiminglin@xjtu.edu.cn

How to cite this article: Lin, Z.; Wang, Y.; Nie, S.; Zou, M.; Xu, F.; Deng, Y.; Lu, Y.; Deng, L.; Li, M.; Luo, G.; Dong, T.; Zhao, L.; Guo, H. Island-bridge microstructured triboelectric pressure sensor for effective dynamic epidermal pulse monitoring. *Soft Sci.* **2025**, *5*, 47. https://dx.doi.org/10.20517/ss.2025.53

Received: 14 Jul 2025 **First Decision:** 31 Jul 2025 **Revised:** 27 Aug 2025 **Accepted:** 2 Sep 2025 **Published:** 19 Sep 2025

Academic Editor: YongAn Huang **Copy Editor:** Pei-Yun Wang **Production Editor:** Pei-Yun Wang

Abstract

Continuous and precise monitoring of pulse waveforms is essential for the prevention and early diagnosis of cardiovascular diseases. However, current pulse sensors suffer from significant motion artifacts caused by inadequate skin-device adhesion and poor interfacial conformability during physical activity. In this work, we develop a highly sensitive and conformal pressure sensor featuring an innovative island-bridge configuration capable of accurately measuring arterial pulse waveforms across multiple body artery sites, even under motion artifacts. Through finite element analysis and systematic experimental validation, the unique island-bridge design is demonstrated in achieving both superior signal fidelity and motion artifact suppression. The developed sensor shows a high-pressure sensitivity of 4.75 V/kPa, a rapid response time of less than 30 ms, and excellent durability over 6,000 cyclic loads. Furthermore, it has demonstrated exceptional performance in capturing pulse waveforms across multiple body sites, allowing the extraction of crucial cardiovascular parameters, even in the presence of motion artifacts. Given the remarkable advantages, our study presents a unique triboelectric sensor design that not only improves the sensitivity but also effectively eliminates motion artifacts, providing a promising solution for creating wearable pressure sensors for continuous cardiovascular monitoring.

Keywords: Triboelectric nanogenerator, triboelectric sensor, self-powered sensor, pulse monitoring

INTRODUCTION

Cardiovascular diseases (CVDs) claim approximately 17.9 million lives annually, representing 32% of global mortality reported by the World Health Organization (WHO)[1-4]. Pulse wave analysis serves as a critical window into cardiovascular health, providing real-time access to hemodynamic parameters that are fundamentally linked to CVD pathogenesis[5-7]. The peripheral arterial waveform encodes multiple clinically relevant features, including pulse wave velocity (PWV), augmentation index (AIx), and diastolic decay time, which are related to CVDs. Continuous pulse monitoring enables detection of dynamic abnormalities, such as the disappearance of the dicrotic notch in aortic stenosis or elevated PWV variability (> 12%) preceding hypertensive crises that manifest hours before acute events. Recent breakthroughs in wearable sensors based on piezoresistive[8-10], capacitive[11-13], piezoelectric[14,15], triboelectric[16-18], and photoelectric types[19,20] enable continuous and real-time pulse wave monitoring, which could revolutionize preventive cardiology by enabling early intervention when arterial remodeling remains reversible. However, existing wearable pulse sensors rarely take into account the body motion artifacts, primarily due to inadequate skin-device interfacial conformability and weak adhesion forces, which are regarded as the critical barrier to precise and reliable cardiovascular monitoring.

Recent studies have explored various strategies to mitigate motion artifacts in pulse monitoring sensors, such as structural design and signal processing techniques[21,22]. For instance, Pang *et al.* demonstrated a flexible pressure sensor with signal amplification from microhair interfacial structures, which shows 12 times enhancement in signal-to-noise ratio via maximization of effective contact between the sensors and the irregular surface of the epidermis[23]. Nevertheless, the microhair structure is highly prone to causing material fatigue failure, leading to a decline in sensor performance. Besides, Biswas *et al.* presented a deep learning framework to efficiently estimate heart rate (HR) information and perform biometric identification using a wrist-worn photoplethysmography (PPG) in an ambulant environment[24]. However, the signal processing method is based on the premise that the acquired physiological signals can be accurately identified, and the coupling of external interference signals with pulse signal will further increase the difficulty of signal processing. Therefore, it is highly important to explore the motion artifact removal techniques for accurate cardiovascular monitoring.

Island-bridge structure, as the typical design in flexible/stretchable electronics, enables uniform distribution of rigid sensors on a flexible substrate, providing an efficient approach for conformal attachment to the human epidermis and interface contact. Han *et al.* has reported a series of novel flexible health monitoring devices and systems based on fractal designs, serpentine electrodes, and discrete functional components. For example, a soft electronic array in multilayer configurations on endocardial balloon catheters is demonstrated, which can establish conformal contact with curved tissue surfaces, support high-density spatiotemporal mapping of temperature, pressure, and electrophysiological parameters[25]. Fewer explorations are taking advantage of the unique island-bridge structure for conformable design in pulse sensors to effectively mitigate the interference caused by motion artifacts.

Herein, we present a triboelectric pulse wave sensor employing the island-bridge configuration for precise arterial pulse measurement, which is designed to meet application requirements for effectively suppressing motion artifacts. Leveraging the island-bridge design, the triboelectric sensor enables complete conformal attachment on human skin to respond to the tiny human pulse due to the enhancement of mechanical compliance. Specifically, the output performance of the sensor also improved, resulting in large elastic deformation to full contact-separation between triboelectric layers. To investigate the distinct advantage of the triboelectric sensor, the mechanical and electrical behavior were theoretically calculated by a finite element analysis (FEA) to obtain a more quantitative understanding of the sensing mechanism. The output

performance of the flexible pressure sensor was characterized depending on various force/frequency modes and process conditions, showing preeminent properties, including a sensitivity of up to 4.75 V/kPa, a response time of less than 30 ms, and remarkable stability after 6,000 cycle tests. A triboelectric sensor was used to detect pulse waves on the human wrist, neck, and fingertip, and such pulse characteristics, including the K value, Alx, PWV, and other key metrics, can be analyzed. Furthermore, the sensor reveals the feature of avoiding motion artifacts for capturing pulse waveforms from the human wrist and fingertip, which provides an insightful approach to overcome the long-standing challenge in motion monitoring and promote the development of personalized cardiovascular care.

EXPERIMENTAL

Materials

Indium tin oxide (ITO, $In_2O_3{\cdot}SnO_2$) and polyethylene terephthalate [PET, $(C_{10}H_8O_4)n$] were purchased from Xingyuan Technology Co., Ltd. (Huizhou, China). Fluorinated ethylene propylene (FEP) was purchased from Chenguan Plastic Industry Co., Ltd. (Taizhou, China).

Preparation of the island-bridge configuration

A layer of FEP film with a thickness of 0.05 mm was sequentially cleaned using menthol, isopropyl alcohol, and deionized water to remove surface contaminants. Following the cleaning process, a high-precision automatic computer numerical control (CNC) laser engraving machine was employed to engrave the FEP film, with the configured parameters including engraving speed of 11.5 mm/s, step distance of 0.5 mm, power of 20 W, and repetition number of 8. Then the patterned island-bridge configuration [Supplementary Figure 1] was formed with the specific dimensional parameters including the bridge length of 0.8 mm, bridge width of 0.1 mm, space of 0.3 mm, and the hexagonal side length of 1 mm.

Fabrication of the island-bridge microstructured triboelectric sensor

The FEP and PET films were selected as the triboelectric layers. A layer of conductive ITO was deposited on the PET substrate with a thickness of 0.05 mm to serve as the electrode. A layer of polyimide (PI) adhesive film was applied along the lateral edges of the PET layer to act as the spacer, ensuring the contact-separation process. The patterned FEP layer was then laminated onto the PI layer. The copper wire was used to connect with the ITO electrode to acquire the pulse signal and was routed to external circuits.

Experimental setup for output characterization

A custom-built testing platform was established to evaluate the performance of the island-bridge microstructured triboelectric sensor (IBTS). A linear motor (LinMot P10-70) was employed to apply programmable dynamic pressure to the IBTS. The real-time output voltage signals were recorded using an electrometer (Keithley Model 6514), synchronized with pressure inputs via a multifunction data acquisition card (NI USB-6218 BNC). The applied pressure values were simultaneously monitored using a digital force gauge (MARK-10), ensuring accurate correlation between mechanical stimuli and sensor response.

RESULTS AND DISCUSSION

Structure design and principle

Figure 1A demonstrates the configuration of the IBTS for cardiovascular monitoring in a movement condition. The triboelectric layer is constructed as an island of hexagons and a bridge of zigzag shape, leaving a tiny gap among the hexagons. The gaps can effectively reduce the elastic modulus of the IBTS, thereby enhancing its capacity for elastic deformation, which will achieve a deformation and displacement for the triboelectric layer. In the design, the PET and FEP are chosen as the triboelectric layers due to their different capabilities of capturing electrons. The ITO was used as the electrode, applied via spin coating onto the PET substrate. A layer of PI tape was adhered between the two tribo-layers as the supporter to

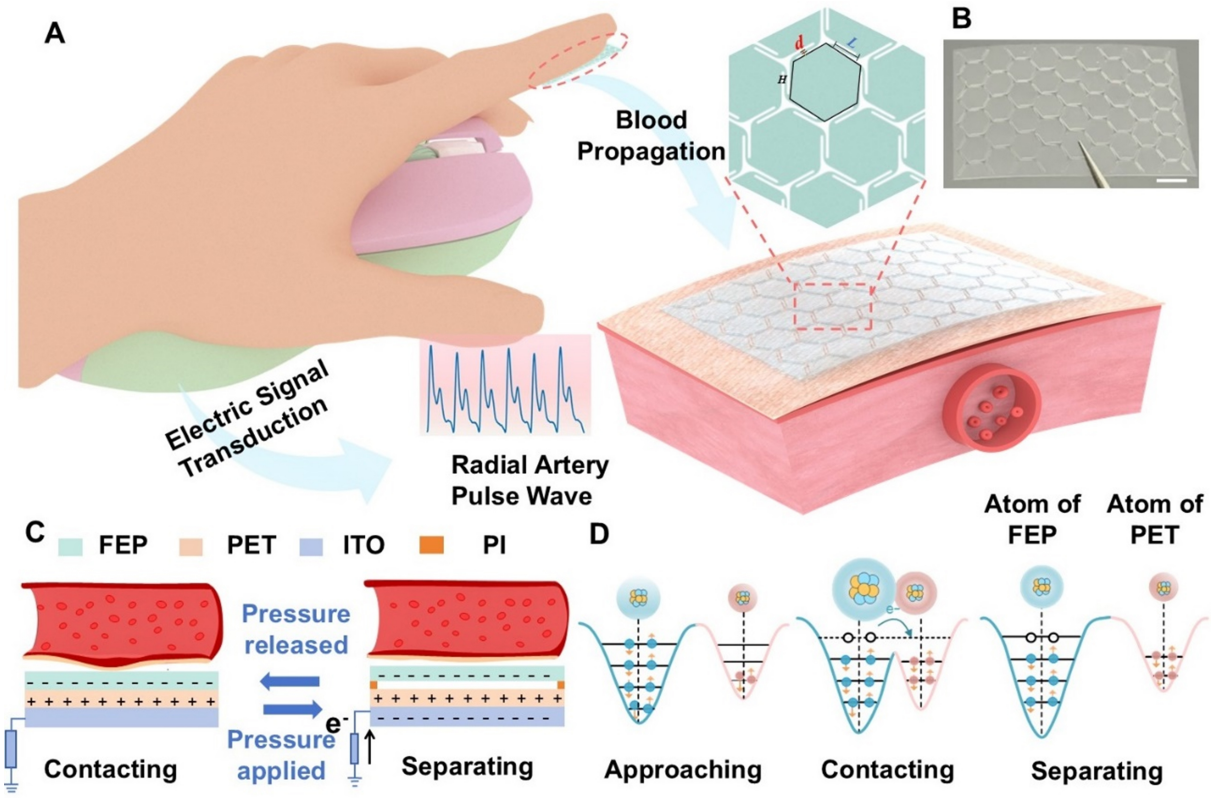

Figure 1. Island-bridge triboelectric sensor for cardiovascular monitoring. (A) Schematic illustration of the sensor's structure design while attached to human fingertip for epidermal pulse monitoring; (B) Photo of the island-bridge configuration (Scale bar: 2 mm); (C) Operating mechanism of the sensor in single-electrode mode; (D) Schematic representation of the atomic potential energy distribution between FEP and PET films before contact, during contact, and separation. FEP: Fluorinated ethylene propylene; PET: polyethylene terephthalate.

achieve contact-separation with the external forces. An as-prepared FEP and IBTS with dimensions of 14 × 24 mm is illustrated in Figure 1B and Supplementary Figure 2, respectively. The detailed fabrication procedures of the IBTS are presented in the Experimental Section.

Figure 1C illustrates the detailed working principle of IBTS, which relies on the coupling effect of contact electrification and electrostatic induction. When external pressure induced by vascular tension is applied to the IBTS, the tribo-layers of PET and FEP films come into contact, and the negative charges will accumulate on the surface of the FEP film, while positive charges are retained on the PET surface due to the differences in triboelectric properties. As the heart transitions into diastole, the vessel wall undergoes elastic recoil, causing the skin to relax, which will lead to the separation of the tribo-layers and generate a potential difference between the electrode and the reference ground. To achieve the potential equilibrium, the potential difference will drive the free electrons from the ground toward the electrode, generating a positive electric current. During the subsequent systolic expansion phase, a negative electric current will be generated due to electrostatic equilibrium. Consequently, the periodic pulse wave could induce synchronized electrical outputs, enabling continuous real-time monitoring of the pulse signal. Besides, Figure 1D illustrates the microscopic process of electron transfer as the two tribo-layers come into contact, thereby elucidating the underlying mechanism of contact electrification. The electron can hop from the PET atom to the PTFE atom due to the overlap of electron clouds, which leads to positively charged PET and negatively charged PTFE.

Finite element simulations

To systematically evaluate the mechanical feasibility of the island-bridge configuration, we performed comprehensive finite element simulations using COMSOL Multiphysics' Solid Mechanics module. The simulation strategy incorporated multiple boundary conditions to rigorously compare the mechanical responses across different sensor architectures. Leveraging the inherent geometric symmetry of the sensor design, we implemented an efficient quadrant-based modeling approach that not only reduced computational overhead but also enabled precise quantitative analysis of stress distribution and deformation characteristics. As shown in Figure 2A and B, the three-dimensional solid mechanics models of both the island-bridge and non-structured configurations were constructed with a coordinate system originating from the upper-left corner. Fixed constraints were applied to two adjacent edges (X = 0 and Y = 0 boundaries), while the other boundaries remained free. Under identical geometric constraints, a vertical external load of 1 Pa was applied normal to the geometric center of each model to simulate mechanical vibration under pulse-like pressure. The unstructured design showed a maximum displacement of 42.5 μm and an average displacement of 11.3 μm, as depicted in Figure 2A. In contrast, the island-bridge design exhibited a maximum displacement of 69 μm and an average displacement of 19.5 μm, as shown in Figure 2B. The average displacement of the island-bridge configuration is approximately 1.7 times greater than that of the unstructured design. Such results highlight the enhanced mechanical deformability provided by the island-bridge design. Similarly, the deformation and stress distribution of the different designs were also performed using COMSOL Multiphysics, as shown in Figure 2C and D. The unstructured design experiences stress concentrated at the center and along its boundaries [Figure 2C]. The island-bridge design shows a different stress distribution, with the majority of stress localized at the connecting regions between hexagonal units [Figure 2D]. This indicates that the localized stress does not significantly hinder the deformation of individual hexagons for external pressure load, which significantly enhances the local deformability, degrees of freedom, and mechanical compliance, allowing the sensor to better conform to the skin, such as the wrist or neck.

To comprehensively understand the contact electrification process of the IBTS, a parallel-plate capacitor using the electrostatics module was modeled. An initial gap of 1 mm was established between the FEP and PET tribo-layers. The simulated potential distributions for different designs are presented in Figure 2E and F, respectively. The results show that the unstructured sensor generates a maximum open-circuit voltage of 41.2 mV and an average of 22.2 mV. In contrast, the maximum open-circuit voltage of the island-bridge design reaches 68.8 mV, with an average output of 36.3 mV, which is approximately 1.6 times that of the unstructured one. Such simulation results demonstrate the effectiveness of the island-bridge configuration in enhancing mechanical deformability and electrical output performance. Overall, the simulations and comparative experiments confirm that the geometric design of the island-bridge configuration optimizes the sensor's mechanical compliance, making it highly suitable for high-sensitivity pressure sensing and minimizing motion artifact interference.

Performance evaluation

To systematically investigate the electrical output characteristics of the IBTS, a test platform was established, integrating dynamic pressure excitation with synchronized signal acquisition, as demonstrated in Supplementary Figure 3. Figure 3A presents a comparison of output voltages for different structural configurations under the same test conditions. The island-bridge-based sensor exhibited a markedly enhanced output voltage of 7.6 V under the applied pressure of 1.5 kPa at a frequency of 1 Hz, which is approximately 3.3 times higher than that of the unstructured sensor. This is ascribed to the island-bridge configuration that enables a higher mechanical deformation of the sensor with a large effective contact area under tiny external stimuli. Additionally, the frequency response characteristics of the IBTS on the output performance were studied, as demonstrated in Figure 3B and Supplementary Figure 4. The IBTS shows

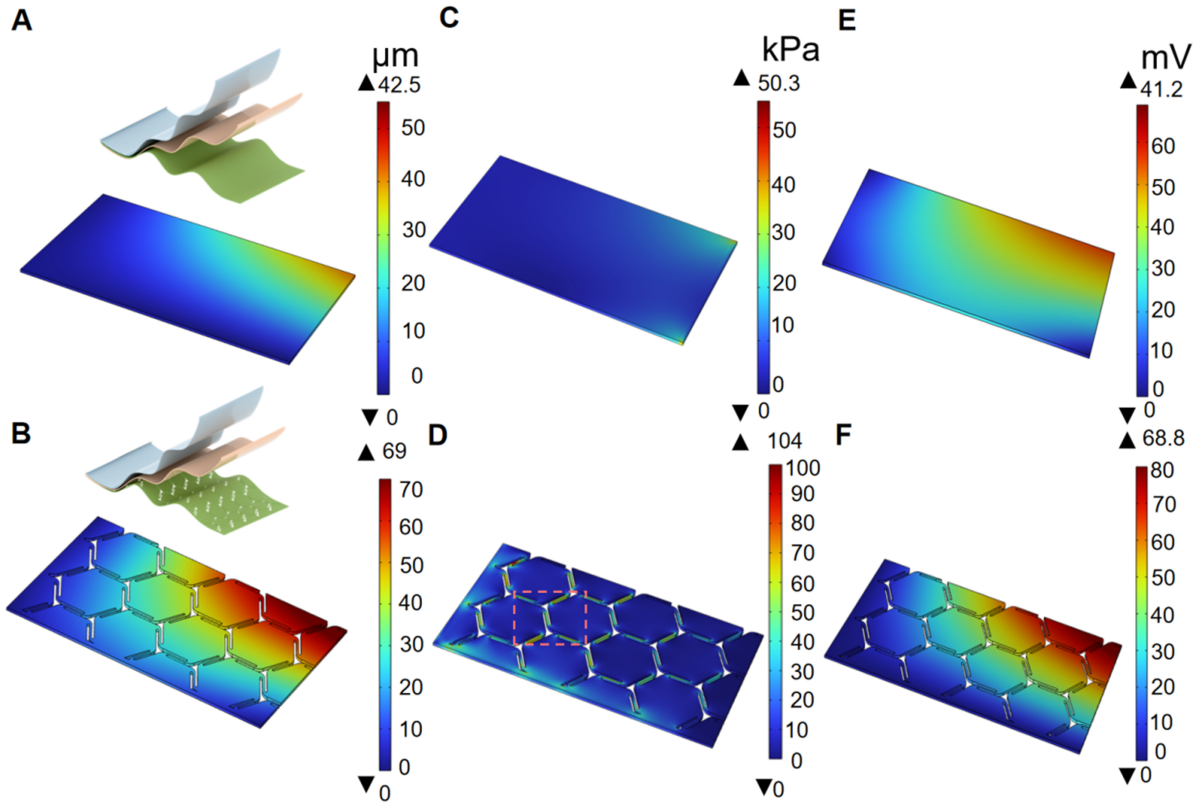

Figure 2. FEA of the mechanical and electrical behavior of the sensor. (A and B) Displacement distribution of the unstructured and island-bridge designs when a pressure of 1 Pa is applied; the inset illustrates the schematic of the two designs; (C and D) Stress distribution of the unstructured and island-bridge designs under an applied pressure of 1 Pa; (E and F) Simulated potential distributions of the unstructured and island-bridge designs. FEA: Finite element analysis.

consistent voltage outputs under constant pressure across the tested frequency range, which highlights its potential for real-time monitoring of the human pulse wave in the required response range, enabling accurate detection of critical waveform features such as tidal and percussion waves. Moreover, the sensitivity was systematically evaluated under varying pressure conditions at a constant frequency of 1 Hz, as shown in Figure 3C. There exist two pressure response regions: the low-pressure and high-pressure regions. The output voltage increases linearly with the low-pressure region of 0-1.5 kPa, exhibiting a sensitivity of up to 4.75 V/kPa; then the voltage increases slowly due to the saturation of the effective contact area of the tribo-layers, resulting in a reduced sensitivity of 0.88 V/kPa in the high-pressure region of 1.5-3 kPa. Besides, the inset reveals that the sensor possesses a minimum detectable pressure as low as 0.1 kPa, underscoring its ability to accurately capture weak mechanical signals and confirming its suitability for applications such as human pulse wave monitoring.

To evaluate the output performance of the IBTS for environmental adaptation, a series of tests was conducted to simulate various environmental disturbances, including continuous air blowing, repeated folding, and torsional deformation, as shown in Figure 3D. The output voltage shows a slight performance attenuation, rendering exceptional mechanical flexibility and environmental adaptation. Besides, Figure 3E illustrates the response time of less than 30 ms for the IBTS, highlighting the capability for timely and accurate pulse wave monitoring. Owing to the curved characteristic of human epidermis, the performance of the sensor was tested on substrates with different bending radii, as shown in Figure 3F. It can be seen that the sensor maintained stable output voltages across all tested curvatures, with no significant performance

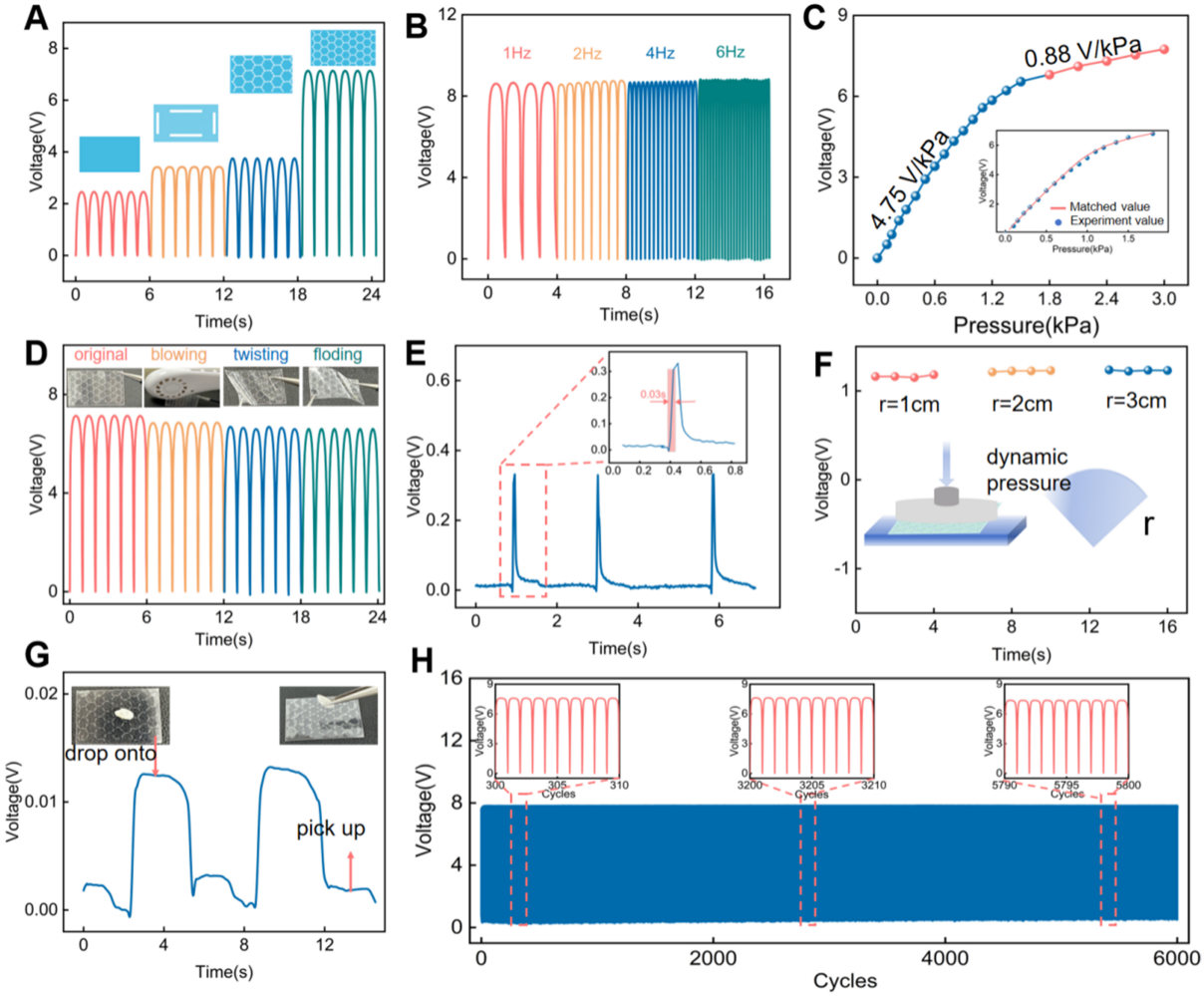

Figure 3. Electrical performance of the IBTS. (A) Output voltage comparisons for different structural configurations; (B) Output voltage of the sensor as a function of excitation frequency; (C) Relationship between output voltage and applied pressure; (D) Output performance for different conditions, including continuous airflow, 200 cycles of folding, and torsion beyond 200 degrees; (E) Response time characterization of the sensor; (F) Output voltage variations under different bending radii (1, 2, and 3 cm); (G) Detection of ultra-low pressures: A stable electrical signal was recorded when a 0.02 g grain of rice was placed on and removed from the sensor; (H) Mechanical durability test for 6,000 cycles of loading and unloading pressure. IBTS: Island-bridge microstructured triboelectric sensor.

degradation, further supporting its potential for conformal and reliable operation in practical pulse wave monitoring. To further assess the sensitivity of the IBTS to subtle pressure changes and validate its applicability for detecting weak physiological signals, a performance test was conducted using a single grain of rice (approximately 0.03 g) as the pressure source, as shown in Figure 3G. As the rice was dropped on and picked up, the sensor surface generated a discernible output voltage of approximately 0.015 V, highlighting the sensor's high sensitivity to minimal mechanical stimuli and potential for monitoring weak physiological signals. Therefore, a durability test was conducted, which involved 6,000 loading and unloading cycles under a constant pressure of 1.5 kPa, as shown in Figure 3H. The output voltages showed no noticeable degradation in signal amplitude or waveform, confirming the sensor's outstanding repeatability and mechanical robustness to satisfy the requirements of continuous pulse wave monitoring.

Continuous monitoring of the pulse wave enabled by the IBTS

Owing to the high sensitivity in detecting subtle physiological signals, the IBTS can be used across various anatomical locations to monitor tiny pulse waves for continuously evaluating the cardiovascular condition, because the pulse waves result from the combined effects of the heart, artery functions, and blood flow. And key waveform features [Supplementary Figure 5], including the P_1 (percussion wave peak), P_2 (tidal wave peak), and P_3 (dicrotic wave peak), are critical for the analysis of cardiovascular indices and serve as important markers for clinical diagnosis. Figure 4 shows the measured pulse waves where IBTS were positioned on the neck, ear, wrist, and fingertip to monitor the carotid, temporal, radial, and digital arteries, respectively. In the experimental results, the pulse waves across different anatomical sites show subtle variations, which reflect the combined effects of vascular distance, arterial elasticity, and wave reflection phenomena. For instance, the carotid artery, located closest to the heart, reflects central arterial pressure and is characterized by a steep, high-amplitude P_1 wave, a minimal P_2 component, and a well-defined P_3 [Figure 4A and Supplementary Movie 1]. In contrast, the auriculotemporal artery near the ear exhibits a lower and flatter P_1, a more prominent P_2, and high-frequency oscillations during the descending phase, attributable to increased peripheral vascular resistance [Figure 4B]. Besides, the radial artery at the wrist, being moderately distant from the heart, shows a slightly attenuated P_1, a more distinct P_2, and a less pronounced P_3 due to interference from peripheral wave reflections [Figure 4C and Supplementary Movie 2]. In addition, the fingertip pulse, transmitted through the distal branches of the brachial artery, presents a small, flattened waveform with a delayed P_1, a reduced P_2, and a smoother, broader P_3 [Figure 4D]. Similar experimental results were also observed in ankle pulse waves [Supplementary Figure 6]. Besides, Supplementary Table 1 and Supplementary Figure 7 show the measured pulse waves for different individuals with a diverse range of ages, genders, and BMI values, which indicated that the IBTS maintains high signal quality across a broad spectrum of users, including those with thicker soft tissue layers or weaker pulses.

Importantly, some vital parameters can be analyzed from the pulse wave to provide a reliable and well-established biomarker for the early diagnosis and risk assessment of cardiovascular conditions [Supplementary Note 1][26,27]. Figure 4E shows the PWV, which is the speed at which these waves travel along the arterial system. In the experiment, a 25-year-old male subject had a PWV of 9.03 m/s, which is within the normal physiological range, indicating preserved arterial elasticity. Besides, AIx, a clinically relevant marker of arterial stiffness, can also be evaluated, as illustrated in Figure 4F. The AIx was calculated as the ratio of the pressure difference between P_2 and P_1 in the pulse wave, and the volunteer's AIx was 64%, consistent with normal values for healthy young adults. Meanwhile, the HR and K values were calculated from pulse wave monitoring at the neck, ear, wrist, and fingertip, as illustrated in Figure 4G. HR and K value could reflect the mean arterial blood pressure, implying a healthy arterial status for the subject. Furthermore, the systolic-diastolic time interval, commonly referred to as the pulse propagation time (PPT), was measured as the temporal difference between characteristic fiducial points in the arterial waveform, as demonstrated in Figure 4H. In addition, the corresponding fast Fourier transformation results shown in Supplementary Figure 8 indicate that the harmonic components of the collected pulse wave were mainly distributed in the range of 0-5 Hz, corresponding to that of healthy adults. Such vital parameters provide significant correlation with the health status of the human cardiovascular system.

Pulse wave monitoring with motion artifacts

To evaluate the capability of IBTS for pulse wave monitoring in real-life conditions, the radial pulse waves were measured from different exercise states, as demonstrated in Figure 5A. The radial artery waves were recorded from the wrist of a 25-year-old male volunteer for pre-exercise and post-exercise conditions. It indicates that HR of 72 beats per minute (bpm) in rest state increased to 30 bpm after 30 min of jump exercise, accompanied by marked changes in waveform morphology, such as the P_2, P_3 peaks, and Time to

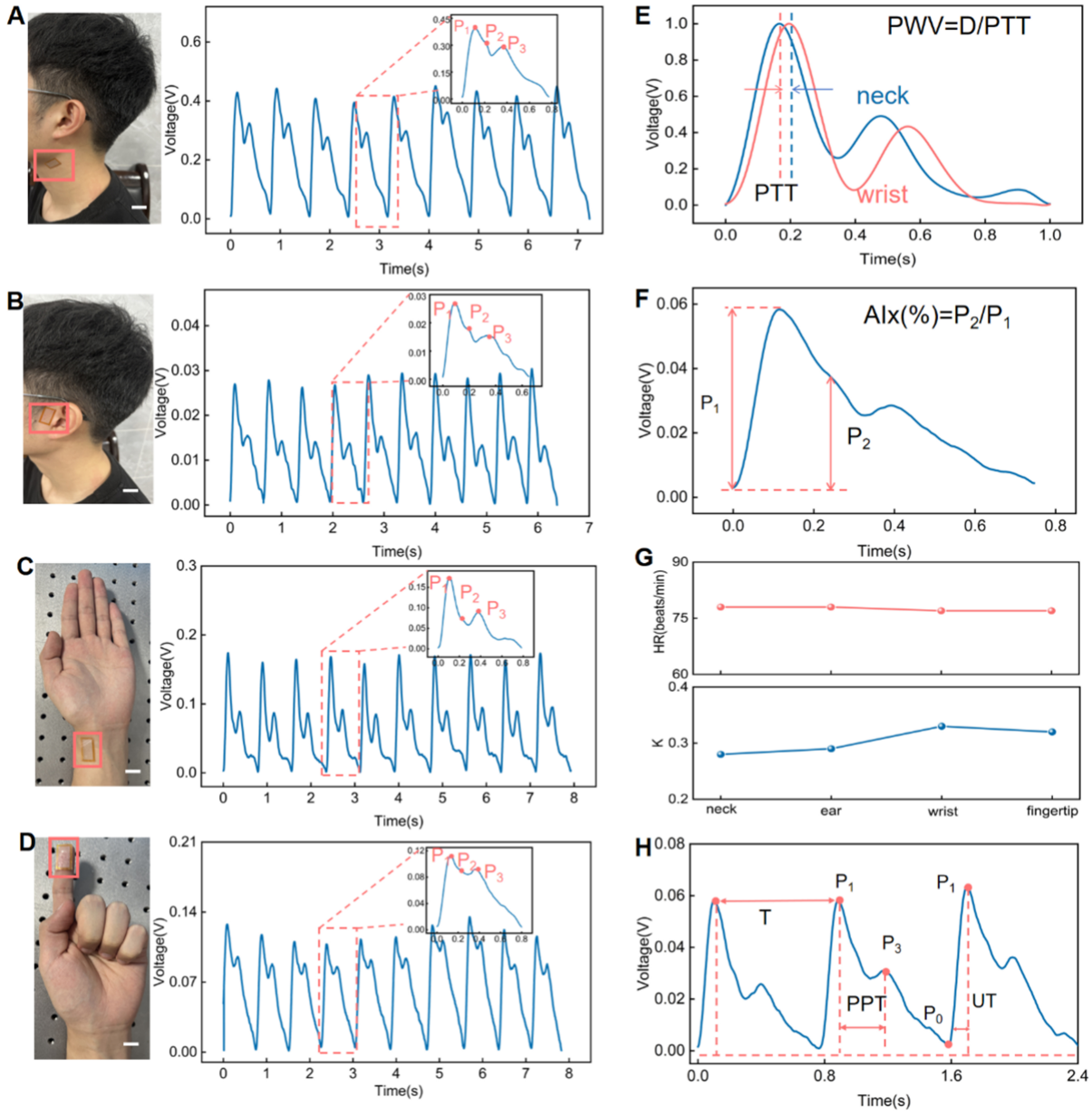

Figure 4. Arterial pulse wave monitoring using the IBTS. (A) Pulse wave monitoring at the neck of a 25-year-old male volunteer using the sensor; (B) pulse wave monitoring at the superficial temporal artery (ear region); (C) pulse wave monitoring at the radial artery of the wrist; (D) pulse wave monitored at the fingertip (Scale bar: 2 cm); (E) PWV measurement based on carotid-radial pulse transit time; (F) The AIx estimation based on the radial artery waveform; (G) HR and K-value derived from pulse wave signals at the neck, ear, wrist, and fingertip; (H) PTT obtained from the radial artery pulse waveform. IBTS: Island-bridge microstructured triboelectric sensor; PWV: pulse wave velocity; AIx: augmentation index; HR: heart rate; PTT: pulse transit time.

peak velocity (Tdvp), which refers to the time interval from the onset of systole to the appearance of peak diastolic blood flow velocity in the heart. Besides, we introduce the Poincare Section diagram for the visual analysis of pulse wave characteristics, which is a nonlinear dynamic approach for analyzing time series data and is widely used in the analysis of physiological signals, such as heart rate variability (HRV) and pulse wave analysis[28-30]. We plotted the HR values obtained from the pulse wave images monitored from a 25-year-old volunteer before and after exercise, as demonstrated in Figure 5B and C. At rest, the Poincare geometry exhibited a standard comet-like shape, with RRn values ranging from 0.75 to 0.9 s (normal range:

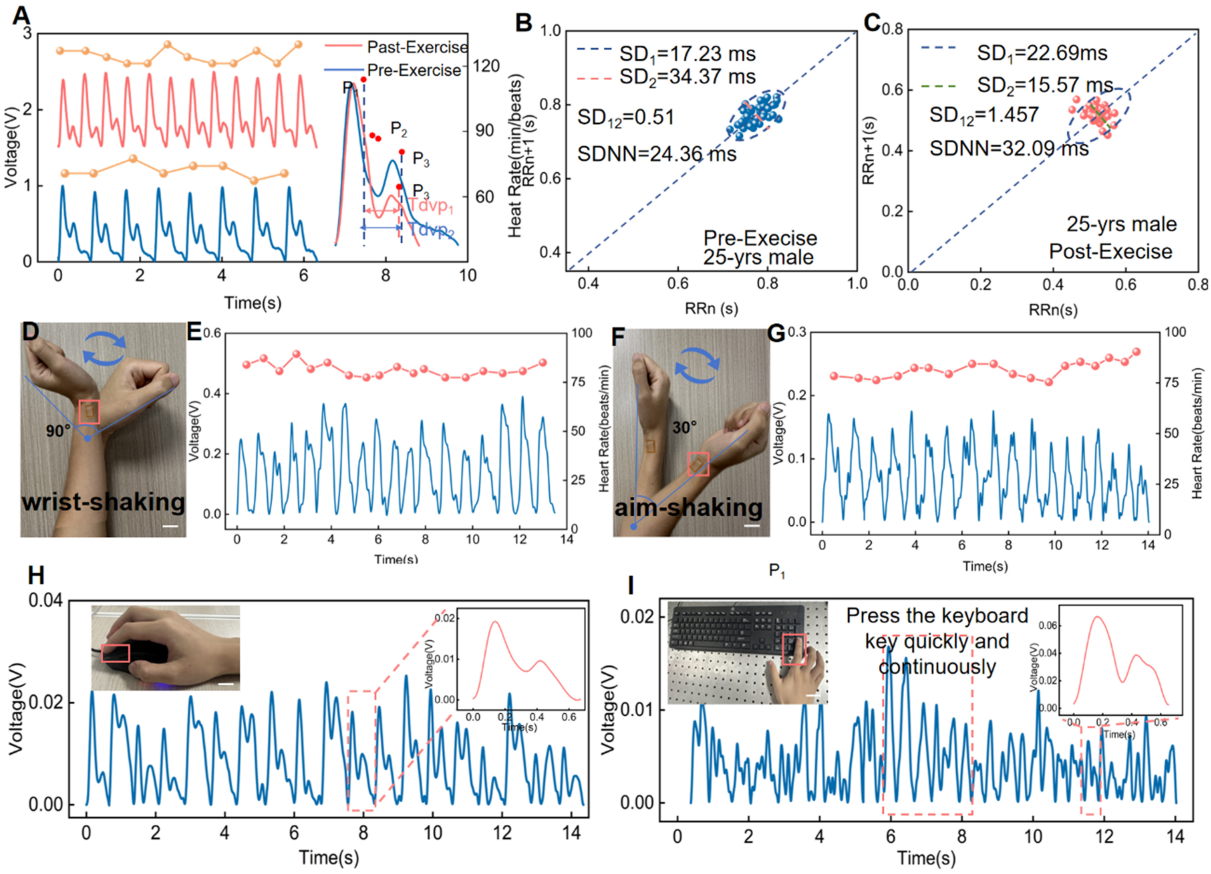

Figure 5. Motion artifact sensing based on the IBTS. (A) Pulse waveforms recorded from the wrist of a 25-year-old male volunteer at rest and after exercise; (B) HR-related parameters of a 25-year-old male volunteer at rest; (C) HR-related parameters of a 25-year-old male volunteer after exercise; (D) The IBTS was attached to the wrist to perform pulse wave monitoring under 90-degree wrist rotation (Scale bar: 3 cm); (E) Radial artery pulse wave monitoring during exceeding 90-degree wrist rotation; (F) The IBTS was attached to the wrist to perform pulse wave monitoring under 30-degree arm swing (Scale bar: 3 cm); (G) Radial artery pulse wave monitoring during 30-degree arm swing; (H) Pulse wave measured from the fingertip while the volunteer was using the mouse (Scale bar: 3 cm); (I) Pulse wave measured from the fingertip while the volunteer was using the keyboard (Scale bar: 3 cm). IBTS: Island-bridge microstructured triboelectric sensor; HR: heart rate.

0.6 to 1 s). SD_1, SD_2, and SD_{12} were recorded as 17.23, 34.37, and 0.51 ms, respectively. It indicates that the cardiovascular system was resting before exercise, characterized by a stable HR and a more consistent pulse wave signal. However, the subsequent values after the exercise for SD_1, SD_2, and SD_{12} were recorded as 22.69, 15.57, and 1.457 ms, respectively [Figure 5D]. This indicates that the cardiovascular system is in an active state, with an accelerated HR and increased variability in the pulse wave signal, reflecting enhanced regulation of the heart and blood vessels.

Despite considerable progress in wearable pulse monitoring technologies, existing pressure sensors remain inadequate for reliably capturing subtle pulse signals during daily activities due to limitations in skin conformability and susceptibility to motion artifacts. These artifacts pose a critical challenge in CVD monitoring, often resulting in signal distortion and, consequently, clinical misinterpretation or diagnostic errors. To assess the capacity for suppressing the motion artifacts, the IBTS was affixed to the radial artery of a 25-year-old male volunteer. The wrist was subjected to repetitive movements exceeding 90 degrees [Figure 5D and Supplementary Movie 3]. Figure 5E presents the acquired pulse wave and corresponding HR data during the movements, and highlights the distinct P_1, P_2, and P_3 characteristic points of the pulse

wave with a stable HR maintained at 80 bpm. Besides, Figure 5F shows that the arm was engaged in a swinging motion exceeding 120 degrees, which introduced greater amplitude compared to typical wrist movements, leading to significant deformation from motion artifacts. The pulse wave can also be recorded with clear P_1, P_2, and P_3 feature points during arm activity under the HR of 78 bpm [Figure 5G]. Such experimental results illustrate that the proposed device can be successfully applied in pulse measurement under motion artifacts.

Importantly, the IBTS was used for continuous pulse wave measurement under various environmental conditions for real-life CVD monitoring. In this study, we integrated the IBTS into two commonly used daily objects, a computer mouse and keyboard, to evaluate its real-world adaptability. Mechanical motion signals typically span a broad frequency range (5-50 Hz) and display irregular amplitude variations. In contrast, human pulse waves are stable, low-frequency signals (0.5-3 Hz) with strong periodicity, corresponding to a HR of 60-180 beats per minute [Supplementary Figure 8]. Therefore, the pulse signals can be extracted by leveraging a 0.5-3 Hz bandpass filter. Figure 5H and Supplementary Movie 4 show the pulse wave acquired from the finger when the volunteer used the mouse. It can be seen that the pulse wave is characterized by three distinct and repeatable peaks, rendering the sensitivity and accuracy of IBTS under motion artifacts. Moreover, when mounted on keyboard keys [Figure 5I and Supplementary Movie 5], the IBTS could capture the pulse waves even under gentle fingertip contact. The insert shows the electrical signals generated by mechanical pressure during key presses, further illustrating the sensor's responsiveness under typical user interactions. This versatility facilitates multi-user and multi-environment deployment, thereby advancing the sensor's potential for unobtrusive, real-time cardiovascular monitoring in daily life.

CONCLUSIONS

We developed a triboelectric pulse sensor featuring the island-bridge architecture that enables precise arterial pulse monitoring while effectively suppressing motion artifacts. The unique island-bridge design enhances mechanical compliance, allowing for complete conformal attachment to human skin and sensitive detection of subtle pulse waveforms. The proposed sensor exhibits outstanding performance metrics, including a high sensitivity of 4.75 mV/Pa, a rapid response time of 30 ms, and excellent operational stability. The sensor can accurately capture pulse waveforms at multiple measurement sites (wrist, neck, and fingertip), even with heavy motion artifacts, enabling analysis of key cardiovascular parameters. Furthermore, it was further integrated onto the computer mouse and keyboard to capture fingertip pulse information under various mechanical pressures, showing great ability to suppress motion artifacts and to deliver precise, real-time cardiovascular data. This breakthrough represents a significant advancement in wearable cardiovascular monitoring, offering a robust solution to the persistent challenge of motion interference and paving the way for personalized healthcare applications.

DECLARATIONS

Authors' contributions

Conception and design of the study: Lin, Z.; Wang, Y.
Provided administrative, technical, and material support: Lin, Z.; Zhao, L.; Guo, H.
Investigation, formal analysis, and validation: Nie, S.; Deng, L.; Zou, M.; Xu, F.; Lu, Y.
Visualization, validation, formal analysis: Deng, Y.; Dong, T.; Li, M.; Luo, G.

Availability of data and materials

All data are available in the main text or the Supplementary Materials. Information requests should be directed to the corresponding authors upon reasonable request.

Financial support and sponsorship

This work was supported by the National Key Research and Development Project (2024YFB3211900), National Natural Science Foundation of China (Grant no. 52472253), Key Research and Development Project of Sichuan Science and Technology Program (24ZDYF1287), General Program of Chongqing Natural Science Foundation (2022NSCQ-MSX0806), and Young Elite Scientists Sponsorship Program by CAST (2022QNRC001).

Conflicts of interest

Deng, L. is affiliated with International Engineering Company, CNPC Chuanqing Drilling Engineering Company Limited. The other authors declared that there are no conflicts of interest.

Ethical approval and consent to participate

The study complied with local regulations and ethical standards, involving only non-invasive monitoring of bodily motion and physical signals. No sensitive personal data or commercial interests were involved, and the procedure caused no harm to participants, thus qualifying for ethical approval exemption. All human experiments involving pressure sensor testing were conducted with informed written consent from the participant (an author of this study).

Consent for publication

Not applicable.

REFERENCES

1. Baghdadi, N. A.; Farghaly Abdelaliem, S. M.; Malki, A.; Gad, I.; Ewis, A.; Atlam, E. Advanced machine learning techniques for cardiovascular disease early detection and diagnosis. *J. Big. Data.* **2023**, *10*, 144. DOI
2. Tsao CW, Aday AW, Almarzooq ZI, et al; American Heart Association Council on Epidemiology and Prevention Statistics Committee and Stroke Statistics Subcommittee. Heart disease and stroke statistics-2023 update: a report from the American Heart Association. *Circulation.* **2023**, *147*, e93-621. DOI PubMed PMC
3. Ghunaim, A. H.; Vervoort, D.; Elfaki, L. A.; Deng, M. X.; Marquis-Gravel, G.; Fremes, S. E. Disparities in therapies for coronary artery disease with reduced left ventricular ejection fraction. *Vessel. Plus.* **2023**, *7*, 29. DOI
4. Maltos-Gómez, F.; Brito-López, A.; Uriarte-Ortiz, J. B.; Guízar Sánchez, D. P.; Muñoz-Comonfort, A.; Sampieri-Cabrera, R. Association between diet, physical activity, smoking, and ultra-processed food and cardiovascular health, depression, and sleep quality. *Cureus* **2024**, *16*, e66561. DOI PubMed PMC
5. Muthukumar, K. A.; Nandi, D.; Ranjan, P.; et al. Integrating electrocardiogram and fundus images for early detection of cardiovascular diseases. *Sci. Rep.* **2025**, *15*, 4390. DOI PubMed PMC
6. Fan, W.; He, Q.; Meng, K.; et al. Machine-knitted washable sensor array textile for precise epidermal physiological signal monitoring. *Sci. Adv.* **2020**, *6*, eaay2840. DOI PubMed PMC
7. Si, S.; Sun, C.; Wu, Y.; et al. 3D interlocked all-textile structured triboelectric pressure sensor for accurately measuring epidermal pulse waves in amphibious environments. *Nano. Res.* **2024**, *17*, 1923-32. DOI
8. Cao, M.; Su, J.; Fan, S.; Qiu, H.; Su, D.; Li, L. Wearable piezoresistive pressure sensors based on 3D graphene. *Chem. Eng. J.* **2021**, *406*, 126777. DOI
9. Pang, Y.; Tian, H.; Tao, L.; et al. Flexible, highly sensitive, and wearable pressure and strain sensors with graphene porous network structure. *ACS. Appl. Mater. Interfaces.* **2016**, *8*, 26458-62. DOI PubMed
10. Jafarizadeh, B.; Chowdhury, A. H.; Khakpour, I.; Pala, N.; Wang, C. Design rules for a wearable micro-fabricated piezo-resistive pressure sensor. *Micromachines* **2022**, *13*, 838. DOI PubMed PMC
11. Kumar S, Soni A, Kumar A. Evaluation of blood pressure using a flexible and wearable capacitive pressure sensor. *RSC. Adv.* **2023**, *13*, 35397-407. DOI PubMed PMC
12. Javidi, R.; Moghimi Zand, M.; Alizadeh Majd, S. Designing wearable capacitive pressure sensors with arrangement of porous pyramidal microstructures. *Micro. Nano. Syst. Lett.* **2023**, *11*, 13. DOI
13. Kumar A. Flexible and wearable capacitive pressure sensor for blood pressure monitoring. *Sens. Bio. Sens. Res.* **2021**, *33*, 100434. DOI
14. Sagar, P.; Sinha, N.; Shukla, M.; Yadav, T.; Kumar, B. Flexible piezoelectric nanogenerator based on Nd-ZnS nanoplates for human

body movements detection and wearable electronics. *J. Alloys. Compd.* **2025**, *1010*, 178035. DOI

15. Yu, Y.; Zhao, X.; Ge, H.; Ye, L. A self-powered piezoelectric Poly(vinyl alcohol)/Polyvinylidene fluoride fiber membrane with alternating multilayer porous structure for energy harvesting and wearable sensors. *Compos. Sci. Technol.* **2024**, *247*, 110429. DOI
16. Lin, Z.; Zou, M.; Lu, Y.; et al. Device design and data processing strategies for self-powered cardiovascular sensors. *Device* **2025**, *3*, 100726. DOI
17. Chen, J.; Wang, Z. L. Reviving vibration energy harvesting and self-powered sensing by a triboelectric nanogenerator. *Joule* **2017**, *1*, 480-521. DOI
18. Fang, Y.; Zou, Y.; Xu, J.; et al. Ambulatory cardiovascular monitoring via a machine-learning-assisted textile triboelectric sensor. *Adv. Mater.* **2021**, *33*, e2104178. DOI PubMed PMC
19. Jafarizadeh, B.; Chowdhury, A. H.; Islam Sozal, M. S.; Cheng, Z.; Pala, N.; Wang, C. Wearable system integrating dual piezoresistive and photoplethysmography sensors for simultaneous pulse wave monitoring. *ACS. Appl. Mater. Interfaces.* **2024**, *16*, 65402-13. DOI PubMed
20. Yan, J.; Ye, Z.; Shi, F.; et al. Reflection-type photoplethysmography pulse sensor based on an integrated optoelectronic chip with a ring structure. *Biomed. Opt. Express.* **2021**, *12*, 6277-83. DOI PubMed PMC
21. Ding, L.; Wang, Y.; Sun, C.; et al. Three-dimensional structured dual-mode flexible sensors for highly sensitive tactile perception and noncontact sensing. *ACS. Appl. Mater. Interfaces.* **2020**, *12*, 20955-64. DOI PubMed
22. Jahnavi, M.; Sharan, B.; Singh, M.; Uma, B. V.; Maruthy, K. N. Assessment of pulse wave velocity in obese adults using ECG and finger tip photo pulse plethysmography. *Int. Physiol. J.* **2020**, *7*, 66-9. DOI
23. Pang, C.; Koo, J. H.; Nguyen, A.; et al. Highly skin-conformal microhairy sensor for pulse signal amplification. *Adv. Mater.* **2015**, *27*, 634-40. DOI PubMed
24. Biswas, D.; Everson, L.; Liu, M.; et al. CorNET: deep learning framework for PPG-based heart rate estimation and biometric identification in ambulant environment. *IEEE. Trans. Biomed. Circuits. Syst.* **2019**, *13*, 282-91. DOI
25. Han, M.; Chen, L.; Aras, K.; et al. Catheter-integrated soft multilayer electronic arrays for multiplexed sensing and actuation during cardiac surgery. *Nat. Biomed. Eng.* **2020**, *4*, 997-1009. DOI PubMed PMC
26. Song, D.; Miao, J.; Zhang, Y.; Zhu, A. Relationship between estimated pulse wave velocity and the risk of future sarcopenia in middle-aged and older Chinese adults: evidence from the China Health and Retirement Longitudinal Study. *Front. Cardiovasc. Med.* **2025**, *12*, 1494635. DOI PubMed PMC
27. Omboni, S.; Arystan, A.; Benczur, B. Ambulatory monitoring of central arterial pressure, wave reflections, and arterial stiffness in patients at cardiovascular risk. *J. Hum. Hypertens.* **2022**, *36*, 352-63. DOI PubMed
28. Wang, X.; Yang, J.; Meng, K.; et al. Enabling the unconstrained epidermal pulse wave monitoring via finger-touching. *Adv. Funct. Mater.* **2021**, *31*, 2102378. DOI
29. Kumar, R.; Aggarwal, Y.; Nigam, V. K.; Sinha, R. K. Correlation of Poincare plot derived stress score and heart rate variability parameters in the assessment of coronary artery disease. *Biomed. Eng. Appl. Basis. Commun.* **2024**, *36*, 2350040. DOI
30. Meng, K.; Zhao, S.; Zhou, Y.; et al. A wireless textile-based sensor system for self-powered personalized health care. *Matter* **2020**, *2*, 896-907. DOI